Assessment of flow field and sediment flux at alpine desanding facilities

C. Paschmann, J. N. Fernandes, D. F. Vetsch & R. M. Boes

Laboratory of Hydraulics, Hydrology and Glaciology (VAW), ETH Zurich, Zurich, Switzerland

ABSTRACT: This paper deals with flow field and sediment flux measurements at alpine desanding facilities. 3D flow velocities and turbidity were recorded and water samples were taken at three alpine desanding facilities. The samples were evaluated regarding suspended sediment concentration (SSC) and particle size distribution (PSD) in the laboratory. SSC was correlated with turbidity and reliable correlations were found for two facilities. The applied instrumentation and methods proved to be appropriate to assess flow field and sediment fluxes. The results show that the flow field is inhomogeneous in large parts of the basins and that the presence of tranquilizing racks has a strong influence on the flow. PSD revealed a refinement of the mean particle size in streamwise direction. The mass-related trapping efficiency of the desanding facilities was estimated based on calculated sediment fluxes and compared to two different trapping efficiency definitions. The results are briefly compared with a current design guideline.

1 INTRODUCTION

Suspended mineral particles – also referred to as suspended sediments – in the turbine water of medium- and high-head hydroelectric power plants (HPPs) can subject turbines to so-called hydro-abrasion, leading to a considerable decline in efficiency (Padhy & Saini 2011) and to increased maintenance costs to repair or replace turbine parts.

To cope with these problems, desanding facilities are located between the water intake and the head-water way leading to the powerhouse. Their purpose is the reduction of the mean particle size and total mass of the suspended sediments in the turbine water. In desanding facilities, the flow is retarded and temporarily stored, allowing the suspended sediments in the diverted water to settle to the basin bed. In Switzerland, elongated facilities are commonly used (Ortmanns 2006). After the inlet channel, a transition zone precedes the settling basin (Fig. 1 to 3). The deposited sediments are flushed continuously or intermittently. The intensity of hydro-abrasion is directly related to the efficiency of desanding facilities, representing a key factor for the sustainable and economic operation of HPPs.

Investigations of Ortmanns (2006) revealed that the flow field in the basin is often inhomogeneous and that the turbulence intensities are significantly higher in the inlet than in the outlet sections. This is in contrast to the assumptions made in current design guidelines, where the approaching flow is assumed to be fully developed channel flow (e.g. Mosonyi 1956 and Giesecke et al. 2014, 'classical approach'). In reality this is often not fulfilled, however, so that the sediment settling efficiency significantly decreases. In these guidelines, the approach flow conditions upstream of the basin are neglected, being a possible reason for the inhomogeneous basin flow field and insufficient basin length and basin cross section to attain high settling efficiencies. Whilst the current design guidelines virtually solely focus on the basin geometry, sparse design recommendations for the inlet channel and transition zone and their effect on the basin flow field exist.

The findings of Weerakoon & Rathnayake (2007) and Shah et al. (2008) on geometric desanding basin design yielded from experimental model investigations, while the suggestions of Lysne et al. (2003) and Quamar et al. (2014) as well as the results of Simanjuntak et al. (2009) obtained from numerical simulations just give hints for the transition zone design. Further investigations on desanding facilities by means of numerical simulations were conducted by Olsen (1994), Olsen & Skoglund (1994) and Olsen & Kjellesvig (1999) as a part of developing the 3D computational fluid dynamics (CFD) soft-

ware SSIIM. Comparing the simulation results with experimental model tests, they found that flow and sediment transport processes can satisfactorily be modeled with SSIIM. Daneshvari et al. (2012) performed numerical simulations of a desanding facility based on the software packages ANSYS CFX and FLOW-3D by focusing on the velocity fields. A new type of flushing system was proposed, although sediment transport was not considered in the simulations. Moreover, the authors conducted only sparse physical investigations to verify the accuracy of the simulation results, concluding that further field data were required to validate the numerical models.

Composite investigations comparing numerical simulation results with field measurement and laboratory test rig data, respectively, were conducted by Bråtveit et al. (2013) and Nøvik et al. (2014). The former compared flow velocity data from a Norwegian desanding facility measured with an acoustic Doppler current profiler (ADCP) with the simulation results using the CFD software StarCCM+. The latter used flow velocity measurement data recorded with acoustic Doppler velocimeters (ADV) at a physical scale model of a Nepalese desanding facility to validate their simulations, which were also performed with Star-CCM+. Both research groups found that the flow field can be satisfactorily represented and were able to qualitatively reproduce the measured turbulence distribution. Nøvik et al. (2014) furthermore suggested to combine flow velocity and suspended sediment concentration (SSC) measurements to increase the significance of suchlike investigations.

It can be concluded that more research on the effect of the facility geometry and the approach flow conditions onto the basin flow field and sediment settling are needed for a correct design of desanding facilities with optimal sediment settling efficiencies. Therefore, the performance of desanding facilities shall be optimized within the scope of a research project at the Laboratory of Hydraulics, Hydrology and Glaciology (VAW) of ETH Zurich. The optimization potential will be systematically investigated by means of a composite approach, modeling flow and settling processes by numerical simulations based on experimental data obtained from precedent field experiments. The field data will be used for calibration and validation of the numerical model and for the detection of particular aspects such as the influence of the tranquilizing racks or of the inlet channel flow field.

In this paper, field data recorded at the desanding facilities Saas Balen (operated by EnAlpin), Wysswasser (Gommerkraftwerke AG) and Moerel (Swiss Federal Railways) in the Swiss canton Valais are presented. The data comprise 3D flow velocity and suspended sediment related quantities on a dense measurement grid. The measurements at each facility have been conducted over a maximum of five days. For that period it was assumed that the:

- flow field in the desanding facility remained quasi constant taking into account that the design discharge was continuously maintained (which was confirmed by the discharge records of the operators);

- mineralogical composition, shape and size distribution of the particles in the according stretch of water remained constant, as long as no extraordinary flow discharge conditions occurred.

2   MEASURING CAMPAIGN

2.1   Desanding facility characteristics

The three investigated desanding facilities – Saas Balen (Fig. 1), Wysswasser (Fig. 2) and Moerel (Fig. 3) – each feature a weir side intake and two settling basins. The diverted water is conveyed into the basins by means of an inlet channel. Between inlet channel and basin, a transition zone is located which in each case is equipped with tranquilizing racks. Tab. 1 summarizes the basin dimensions length, L, and width, W, the mean flow depth, h, the longitudinal bed slope, J_s, the discharge during the measurements, Q, and the flushing system of the three facilities.

Table 1. Characteristics of the investigated desanding facilities Saas Balen, Wysswasser and Moerel.

Facility	Basin dimensions $L/W/h$	Slope J_s	Discharge Q	Flushing system
[-]	[m]	[-]	[m^3/s]	[-]
Saas Balen	35.00 / 5.80 / 4.95	0	2.2	Bieri (Patt & Gonsowski 2011)
Wysswasser	32.00 / 4.00 / 6.52	0	5.0	HSR (Truffer et al. 2009)
Moerel	43.00 / 8.35 / 4.93	0.01	10.8	Dufour (Patt & Gonsowski 2011)

2.2   Installation and measurement equipment

A modular bearing system for the measurement instrumentation was used at the desanding facilities (Fig. 4). It was composed of a horizontal truss, a trolley and a motorized vertical linear unit. The setup allowed the 3D movement of the measurement instrumentation. Connected to the motorized linear unit, four acoustic Doppler velocimeters (ADVs) Nortek Vectrino+ with side-looking head were used for the 3D flow velocity measurements. The nominal measurement accuracy is ±0.001 m/s ±0.005 times the measured velocity components. In addition, a funnel connected to a hose was also attached to the linear unit at the same elevation as the lowest ADV. The funnel allows for quasi-isokinetic water sampling, controlled by its cross sectional area. A pump enables the withdrawal of water, gathered at the funnel.

A turbidity sensor CUS52D of Endress+Hauser was used for continuous and real-time water turbidity measurements. Its nominal measurement accuracy is 2% ±0.01 FNU (Formazine Nephelometric Units). At the end of that measuring line, water samples for laboratory investigation were collected and stored under refrigerated conditions. To measure the water surface elevation in the basin, a radar sensor Vegapuls 61 of Vega was applied. Additionally, turbidity sensors CUS52D were installed at the inlet channel and at the basin outlet. Further details on the instrumentation and measuring concept may be obtained in Paschmann et al. (2016).

2.3   Measurement procedure

Depending on the investigated facility, measurements were carried out at 9 to 12 cross sections corresponding to 3 to 4 m intervals along the basin. Each cross section contained about 50 to 70 single flow velocity measuring points. In 25% of these points, turbidity was additionally measured. The measurement time was 90 s in each measuring point. The ADVs, the turbidity sensors and the radar sensor sampled at a frequency of 100 Hz. Water samples were intermittently taken in several cross sections at two flow depths along the center line of the basin during the cross sectional measurements.

In the inlet channel and at the outlet, the turbidity measurement and water withdrawal took place at mean flow depth in the middle axis. Regarding turbidity as well as SSC and PSD, these locations are rated as representative for the whole cross section, because the observed fully turbulent flow (Reynolds numbers Re > 10^5) facilitates a homogeneous mixing of water and suspended sediments. Supplemental measurements of flow velocities in a dense measurement grid were also performed in a single inlet channel cross section just upstream of the transition zone.

To determine the PSD, the dried residues of selected bottle samples were investigated in the laboratory with a laser particle size analyzer LA-950 of Horiba Scientific. For the purpose described herein the volumetric output of the measurements was chosen, in line with the standard approach. For example, the characteristic median particle diameter d_{50} is the particle size which is exceeded by 50 volume percent of the particles in an investigated sample.

2.4 Data evaluation

The measurement point coordinates x, y and z were normalized with the basin length L, width W and mean flow depth h, respectively. From this follow $x/L = X$, $y/W = Y$ and $z/h = Z$. The origin of the co-ordinate system was always at the upstream basin end on the invert and at the orographic right wall.

The ADV raw data files were filtered based on the phase-space threshold method proposed by Goring & Nikora (2002) and modified by Wahl (2003) as implemented in the software WinADV. To obtain insights into the turbulent flow structures, the distribution of the turbulent kinetic energy $e_{t,kin}$ (TKE) was evaluated. The TKE is associated with eddies in turbulent flow and is therefore suitable as a simplified measure of flow turbulence within the basin. The TKE is calculated as (Pope 2000):

$$e_{t,kin} = \frac{1}{2} \cdot \left(\overline{v_x'^2} + \overline{v_y'^2} + \overline{v_z'^2} \right) \qquad [\text{m}^2/\text{s}^2] \tag{1}$$

where v_x', v_y', v_z' = turbulent fluctuations [m/s] of the longitudinal, transverse and vertical flow velocity components, respectively.

Following the detailed explanations of Wren (2000) and the findings of e.g. Kühn (2007), Felix et al. (2012) and Boes et al. (2013), a linear correlation of turbidity and SSC can be found if the sediment particles retain consistent characteristics. For the investigated facilities, a linear regression has been carried out for each turbidity sensor (inlet channel, basin and outlet, cf. section 3). In each case, the coefficient of determination, R^2, of the linear regression was evaluated to check the reliability of each relationship.

To assess the present sediment flux, the SSC was calculated with the regression equations based on the measured turbidity. The SSC was then utilized to estimate the sediment fluxes F_S:

$$F_S = SSC \cdot Q \quad [\text{kg/s}] \tag{2}$$

where Q = water discharge [m^3/s].

To draw general conclusions, the cross sectional sediment fluxes $F_{S,x}$ were normalized by the according instantaneous mean sediment flux in the inlet channel $F_{S,in}$ during the measurement of each cross section. Based on the normalized sediment fluxes, the deposition pattern can be estimated by comparing the cross sectional fluxes of consecutive cross sections. An increased sediment flux between two cross sections indicates erosion in between, whilst a decrease may imply deposition. Nevertheless, care has to be taken when interpreting the cross sectional variation of the sediment fluxes. Due to the chosen measurement grid, sediment particles being transported below the lowest measuring point of water withdrawal were not captured during the field measurements.

Moreover, the comparison of the mean sediment fluxes at the inlet channel ($F_{S,in,m}$) and the basin outlet ($F_{S,out,m}$) allowed for the estimation of the mass-related trapping efficiency η_m of the desanding facility:

$$\eta_m = \left(F_{S,in,m} - F_{S,out,m} \right) / F_{S,in,m} \tag{3}$$

In a similar manner to the estimation of the mass-related trapping efficiency, it is possible to check the total sediment mass that is trapped in the desanding facility during the measurements. For that purpose, the sediment fluxes in the inlet channel and the outlet are integrated over the total measurement duration.

In addition to the mass-related trapping efficiency, the critical-particle-size-related trapping efficiency η_{PSD} used in the 'classical' design approach was determined (e.g. Mosonyi 1956). Principally, η_{PSD} can be estimated for all particle sizes occurring in a desanding facility. In practice, it is determined with reference to the so-called critical limit particle size d_{cr}. It is not a universal value, but rather depends on the specific requirements of the operator of each particular desanding facility. Herein, the d_{cr} values calculated according to the 'classical' design approach amount to 190, 305 and 430 μm for the Saas Balen, Wysswasser and Moerel facility, respectively. To estimate η_{PSD}, the fraction w of particles finer than the critical limit particle size is determined based on the averaged PSD in either the outlet, or the last measurement cross section of the facilities, leading to

$$\eta_{PSD} = w(d_{cr})_{out} \tag{4}$$

Furthermore, comparing the median particle size at the inlet ($d_{50,in}$) and the outlet ($d_{50,out}$), the median-particle-size-related trapping efficiency η_{d50} can be used as benchmark for the facility performance. It is calculated as:

$$\eta_{d50} = \left(d_{50,in} - d_{50,out}\right) / d_{50,in} \tag{5}$$

3 RESULTS

3.1 General

Discharge recordings provided by the facility operators show that the measurements at all three facilities were conducted at approximately steady design discharge conditions. The SSC ranged from 0.05 to 2.16 g/l at Saas Balen, 0.18 to 1.09 g/l at Wysswasser and 0.08 to 0.21 g/l at Moerel, taking also the measurements at the inlet channel and the outlet into account. Following the experience of the operators, no exceptional SSC peaks were recorded.

3.2 Saas Balen

Flow field

The flow field was found to be considerably inhomogeneous in large reaches of the basin. About half the basin length is characterized by higher than average flow velocities near the side walls and the bottom (Fig. 5). They are about twice as high as the basin mean flow velocity. In contrast, flow velocities up to half as high as the basin mean flow velocity can be identified in large parts of the water body downstream of the racks, especially in the central flow area and at the water surface. The TKE is reduced by two orders of magnitude (4200 to 30 cm^2/s^2) between the inlet channel and the upstream basin cross section at $X = 0$ (Fig. 6).

Within the second half of the basin, the flow becomes increasingly more homogeneous. Beginning at $X = 0.6$, the cross sectional mean TKE is about 10 cm^2/s^2 and remains almost constant until the basin end (Fig. 6). Between $X = 0$ and $X = 0.94$, the cross sectional mean TKE is reduced by 82%. In the last third of the basin, the velocities approximate the basin mean flow velocity throughout the flow area (Fig. 5).

Fig. 7 shows the flow velocity distribution in the inlet channel measurement cross section upstream of the basin. The measured inlet channel flow velocity v_{in} is normalized by the mean basin flow velocity $v_{basin,m}$. Comparing Fig. 5a and Fig. 7 shows that the main flow tends to change from the orographic right to the orographic left side. Furthermore, the spread of flow velocities is distinctly larger in the inlet channel compared to the basin.

Sediment flux

Fig. 8 (top) shows the correlation of the measured turbidities and gravimetric SSCs for Saas Balen, indicating that reliable linear correlations were found ($0.91 < R^2 < 0.97$). The regression equations are used to determine the SSC and the sediment fluxes (Eq. 2). Fig. 9 shows the normalized cross sectional sediment fluxes (left ordinate) as well as the according simultaneous SSC in the inlet channel (SSC_{in}, right ordinate). The latter is used to calculate the inlet channel sediment flux $F_{S,in}$ for the selected normalization (cf. section 2.4). The mean sediment flux in the inlet channel and in the outlet results in $F_{S,in,m} = 1.64$ kg/s and $F_{S,out,m} = 0.54$ kg/s, respectively. The mass related trapping efficiency thus becomes $\eta_m = 0.67$ according to Eq. (3).

Based on the ratio $F_{S,x}/F_{S,in}$ it can be found that about 30% of the suspended sediments deposit upstream of cross section $X = 0$ and hence in the area of the tranquilizing racks. Furthermore, it can be depicted that about 50% of the entering sediment is trapped at the end of the basin. The first half of the basin is not significantly effective for particle settling.

Following the description in section 2.4, the total sediment mass having passed the inlet channel during the measurements (approximately 21 hours) can be estimated as 102 t, of which 37 t of sediment passed the outlet, leading to a total trapped sediment mass of 65 t. The resulting efficiency was 64%, which is similar to the mass-related trapping efficiency based on mean fluxes.

Besides the reduction of sediment mass along the basin, a refinement of particle sizes can be found based on PSD analyses of the water samples in the inlet channel and the outlet (Fig. 10). The median diameter decreases from $d_{50} = 54$ to 30 μm and the maximum diameter from about $d_{max} = 1000$ to 400 μm. This results in $\eta_{d50} = 0.44$ according to Eq. (5). Analyzing the PSD curves moreover results in $\eta_{PSD} \approx 0.95$ according to Eq. (4), since about 95% of the particles in the outlet are smaller than $d_{cr} = 190$ μm.

3.3   Wysswasser

Flow field

Due to on-site constraints, the first measurement cross section $X = 0.20$ is located 6.45 m downstream of the end of the transition zone. The cross sectional average TKE decreases from 300 cm^2/s^2 in the inlet channel to 60 cm^2/s^2 at $X = 0.2$ (Fig. 6).

Differing from the Saas Balen facility, the flow velocity distribution is rather similar from cross section $X = 0.2$ to $X = 0.66$ (Fig. 11). However, the flow field exhibits significantly higher values of the longitudinal velocity v_x near the bottom. At cross section $X = 0.97$, clearly altered flow conditions can be identified. Very low flow velocities and partial return flow were recorded in the lower reach of the measurement grid, whereas high velocities can be found in the upper reach. The cross sectional average TKE decreases slightly from 60 to 40 cm^2/s^2 between cross sections $X = 0.20$ and 0.84, but increases significantly in the last measurement cross section (Fig. 6), supporting the flow acceleration in the vicinity of the downstream weir.

Sediment flux

At Wysswasser, a limited reliable correlation of turbidity and SSC for the basin was found. Fig. 8 (bottom) exhibits the presence of mainly two point clouds, thus the coefficient of regression ($R^2 = 0.93$) must be interpreted carefully. Also the correlation for the inlet channel has to be used with caution, since only four water samples were evaluated. For the outlet at Wysswasser, too few water samples were usable for laboratory investigation, so that no clear correlation was obtained. Nevertheless, the

sediment fluxes were calculated in analogy to the Saas Balen facility. Fig. 12 shows the normalized cross sectional sediment fluxes as well as the according simultaneous SSC in the inlet channel (SSC_{in}). About 10% of the suspended sediments deposit upstream of cross section $X = 0.20$. In the last third of the basin $F_{S,x}/F_{S,in}$ slightly decreases from 94% to a value of 85%.

Since there is no correlation of turbidity and SSC available for the outlet, the estimation of the mass-related trapping efficiency is based on $F_{S,in}$ and the sediment flux $F_{S,X=0.97}$ at the last basin measurement cross section ($X = 0.97$) for the measurement period of that cross section only. With $F_{S,in} = 4.3$ kg/s and $F_{S,X=0.97} = 3.6$ kg/s, the mass-related trapping efficiency according to Eq. (3) becomes $\eta_m = 0.16$. The total sediment mass having passed the inlet channel during the measurements (approximately 19 hours) can be estimated to be 181 t.

The median sediment diameter decreases from $d_{50} = 37$ to 19 μm and d_{max} from about 400 to 300 μm (Fig. 10), indicating a particle size refinement between the inlet channel and the outlet. The median-particle-size-related trapping efficiency is $\eta_{d50} = 0.48$. The critical-particle-size-related trapping efficiency is virtually $\eta_{PSD} \approx 1.00$, since all particles in the outlet are smaller than $d_{cr} = 305$ μm, calculated according to the 'classical' design approach.

3.4   Moerel

Flow field

The cross sectional average TKE is reduced by 38% between the inlet channel measurement cross section and $X = 0$ (Fig. 6). On the orographic left side, flow velocities tend to be lower when compared to the orographic right side (Fig. 13), which can be attributed to the present distinct left-hand bend of the inlet channel (Fig. 3). However, return flow at the water surface on the orographic right side was observed during the measurement, which can be identified in the measurement data to some extent. This asymmetric flow field persists until about cross section $X = 0.37$. In the further course of the basin, the flow becomes increasingly homogeneous (Fig. 13b). Slightly higher velocities were perpetually recorded at the orographic right side, however (Fig. 13a). The cross sectional average TKE slightly decreases from about 50 cm²/s² at $X = 0.37$ to 25 cm²/s² at $X = 0.93$ (Fig. 6). Considering the whole basin reach, it is reduced by 80%.

Sediment flux

Due to too low SSC during the measurement campaign and its small variance, there is no reliable correlation between turbidity and SSC for the Moerel facility (Fig. 14). The basin SSC was between 0.11 and 0.21 g/l and the turbidity records show rather random values between 75 and 110 FNU, which is a small turbidity spread compared to Saas Balen and Wysswasser facility. Therefore, no sediment flux investigations were conducted for the Moerel facility.

Nevertheless, evaluation of PSD from the basin water samples was possible (note that no data from the inlet and outlet are available). Between the measurement cross sections $X = 0$ and $X = 0.93$, the median particle diameter remained virtually constant at about $d_{50} = 21$ to 24 μm. This also applied for the maximum detected particle diameter, which remained constant at about $d_{max} = 300$ μm. Due to the lack of the required data, η_m cannot be calculated. Since $d_{max} < d_{cr} = 430$ μm and $d_{50} \approx$ const., $\eta_{PSD} = 1.00$ and $\eta_{d50} \approx 0$.

3.5   Facility comparison

Tab. 2 provides an overview over selected measurement data from the three investigated facilities. It contains the variation ΔTKE between the first and the last basin measurement cross section and the

change of the maximum Δd_{max} and median particle sizes Δd_{50}. An increase is indicated by '+', whereas '−' means a decrease of the corresponding parameter. Furthermore, the mass-related (η_m), median-particle-size-related and critical-particle-size-related trapping efficiencies (η_{PSD}) are presented.

Table 2. Overview over selected evaluated measurement data from the three investigated facilities.

Facility	ΔTKE	Δd_{max}	Δd_{50}	η_m	η_{d50}	η_{PSD}
[-]	[cm^2/s^2]	[μm]	[μm]	[-]	[-]	[-]
Saas Balen	− 25	− 600	− 24	0.67	0.44	0.95
Wysswasser	+ 20	− 100	− 18	0.16	0.48	1.00
Moerel	− 100	~ 0	~ 0	---	~ 0 [*]	1.00 [*]

[*] determined between $X = 0$ and $X = 0.93$

3.6 MEASUREMENT ERROR PROPAGATION

Flow velocity

Analyzing the velocity data regarding the nominal measurement accuracy of the ADV probes, the variance of the temporally averaged recorded basin flow velocity magnitudes v_m amounts to about ± 0.002 m/s (≙ 0.017 v_m), ± 0.002 m/s (≙ 0.009 v_m) and ± 0.004 m/s (≙ 0.007 v_m) at Saas Balen, Wysswasser and Moerel, respectively. Applying the same deviation to the calculated root-mean-square values of the turbulent flow velocity fluctuations ($v'_{i,rms}$) results in a TKE variance of about ± 1 cm^2/s^2 for all investigated facilities.

Turbidity and SSC

Since the investigation of the bottle samples took place under laboratory conditions and with reasonable care, the determined gravimetric SSCs are considered as "true". For the applied linear correlations between turbidity and SSC, the measurement deviation due to the turbidity sensor accuracy leads to a maximum SSC variance of ± 0.04 g/l / ± 0.03 g/l / ± 0.01 g/l (inlet channel/basin/outlet) at Saas Balen, and ± 0.04 g/l / ± 0.02 g/l (inlet channel/basin) at Wysswasser, in each case referring to the maximum recorded turbidity.

4 DISCUSSION

4.1 Saas Balen

The flow velocity distribution in the inlet channel measurement cross section (Fig. 7) corresponds to the present left-hand bend of the inlet channel just upstream of the transition zone. Higher velocities were observed at the outside (orographic right side), lower velocities at the inside. However, investigating the basin flow field (Fig. 5), higher flow velocities can be identified at the orographic left side. This change of flow pattern is likely to be caused by the geometric design of the inlet and transition zone as well as the presence of the tranquilizing racks.

Moreover, the racks may cause the presence of the high velocity zones along the fixed boundaries and the zones of quite low flow velocities downstream of the racks. The former may occur since the flow is accelerated in the gaps between the side walls and the basin invert, and the outer edges of the racks, respectively (Fig. 15). The latter most likely occurs because the racks hinder the flow in the central flow area.

The more homogeneous flow field and the lower TKE values appearing from about the half to the last third of the basin have a positive effect on the particle settling, which is expressed in a continuous reduction of cross sectional sediment fluxes (Fig. 9). Although half of the basin exhibits unfavourable flow conditions for particle settling (high level of TKE, non-uniform flow distribution), the overall efficiency is acceptable, since about two-thirds of the sediment mass settles in the basin and the mean and maximum particle sizes are distinctly reduced (Fig. 10).

4.2 Wysswasser

A possible reason for the unexpected flow velocity distribution over the flow depth could be the complex geometry of the transition zone. It is composed of a strongly inclined vertical transition (bed slope 40%) of only 3.7 m length, followed by a vertical backwards facing step of about 2.5 m height. Additionally, the three rows of tranquilizing racks in the transition zone may have an influence onto the flow field (Fig. 16). The racks do not evenly reduce the flow area, but leave blank areas (increasing from row to row) between the bottom end of the rack bars and the bed of the transition zone. In analogy to the findings at Saas Balen, the flow is accelerated in these gaps, featuring a pattern similar to a jet flow. At the end of the basin, the flow field is inverted within depth: higher flow velocities can be found in the upper part close to the water surface, caused by the overfall weir located at the end of the basin. The weir causes a redirection of the flow leading to increased TKE values at the end of the basin (Fig. 6).

The reach from $X = 0.28$ to 0.66 is possibly characterized by significant resuspension of deposited sediments, or an upwards directed sediment flux which was not captured by the measurements in the first third of the basin (Fig. 12). According to the 'classical' design approach (e.g. Mosonyi 1956 and Giesecke et al. 2014), the basin design exactly matches the suggested ratios of length to width and width to flow depth to achieve advantageous flow conditions for the settling of particles $d_{cr} = 305$ μm. Whilst $d_{max} = 300$ μm falls exactly below that threshold, the overall reduction of sediment mass is rather low, resulting in a low mass-related efficiency of $\eta_m = 0.16$ only.

4.3 Moerel

Although four rows of tranquilizing racks are installed in the transition zone, the flow is not significantly homogenized. The left-hand bend of the inlet channel is still reflected in the asymmetric flow velocity distribution in the first third of the basin (Fig. 13). This may be attributed to the comparably high mean approach flow velocity of about 1.6 m/s in the inlet channel.

The insufficient sediment data availability does not allow for obtaining detailed insights regarding the sediment fluxes. Thus, the trapping efficiency can exclusively be qualitatively estimated, leading to values between 0 (η_{d50}) and 1 (η_{PSD}). Nevertheless, following the example of the Moerel facility, the importance to select the appropriate trapping efficiency definition regarding the reduction of hydro-abrasion is clearly demonstrated.

5 CONCLUSION

The flow fields and sediment fluxes were determined at three Swiss desanding facilities using various measurement devices. The employed acoustic Doppler velocimeters (ADVs) are well suited to record 3D flow velocities including turbulent fluctuations at high temporal resolution. A dense measurement grid was used to ensure an adequate spatial resolution, providing valuable insights into the site-specific flow characteristics. For instance, the effect of the tranquilizing racks onto the flow field was clearly identified.

The combination of turbidity measurements and comprehensive water sample analyses yielded several reliable linear regressions to estimate the suspended sediment concentration based on turbidity. Consequently, it was determined for about 200 points within the basins at Saas Balen and Wysswasser and in the inlet channels of both facilities as well as in the outlet at Saas Balen. No sediment flux investigations were conducted for the facility Moerel since no reliable correlations between turbidity and SSC could be found. This was due to rather low SSC during the measurement campaign in combination with its small variance.

Each of the investigated facilities exhibits significant inhomogeneous flow conditions in approximately the first third of the basin. The flow fields were consistently found to strongly differ from assumptions made in current design approaches. Furthermore, TKE is significantly higher at the beginning of the basins compared to the basin end. These disadvantageous flow conditions can be attributed to the inhomogeneous approach flow conditions upstream of the basins. Further downstream, the flow fields become increasingly more homogeneous. The presence of the tranquilizing racks is expressed by a significant reduction of TKE between inlet channel and basin at all facilities. The racks homogenize and align the flow and thus reduce turbulent velocity fluctuations in the downstream reach.

Sediment fluxes were determined based on the cross sectional integration of SSC to assess deposition patterns and transported sediment masses. It could be shown that the mass-related, median-particle-size-related and critical-particle-size-related trapping efficiencies can significantly vary for a given facility. This discrepancy can become crucial when dimensioning desanding facilities. Depending on the chosen approach, the investigated facilities may perform either very well, or poorly. Nevertheless, analyzing the particle size distributions revealed an appreciable decrease in mean particle size and thus a refinement of suspended sediment along the basins at the Saas Balen and Wysswasser facilities.

With regard to the measurement error propagation of flow velocity, turbidity and SSC, the identified data scatter is considered to be insignificant within the scope of the present research. It should be noted that some uncertainty in the data basis exists, since not the whole flow area could be covered by the measurements and because simplifying assumptions were made. Nonetheless, the acquired measurement data are of high quality and are a valuable basis for numerical model calibration and validation.

REFERENCES

Boes, R.M., Felix, D. & Albayrak, I. 2013. Schwebstoffmonitoring zum verschleissoptimierten Betrieb von Hochdruck-Wasserkraftanlagen (´Suspended sediment monitoring for the wear optimized operation of high-head hydroelectric power plants´). *Wasser Energie Luft* 102(1): 35-42 (in German).

Bråtveit, K., Brevik, O. & Olsen, N.R.B. 2013. Three Dimensional Numerical Study of an Unlined Pressurized Rock-Blasted Sand Trap. Proc. *35th IAHR World Congress*, Chengdu, China.

Daneshvari, M., Münch-Alligné, C. & De Cesare, G. 2012. Numerical simulation of a new sand trap flushing system. *Proc. 4th IAHR International Symposium on Hydraulic Structures*. Porto, Portugal.

Felix, D., Albayrak, I., Abgottspon, A., Boes, R.M. & Gruber, P. 2012. Suspended sediment and Pelton turbine wear monitoring: experimental investigation of various optical and acoustic devices and beginning of the case study at HPP Fieschertal. *Proc. 17th Int. Seminar on Hydropower Plants*, Vienna, Austria: 483-494.

Giesecke, J., Heimerl, S. & Mosonyi, E. 2014. *Wasserkraftanlagen – Planung, Bau und Betrieb (`Hydroelectric power plants – Planning, construction and operation')*, Springer, Berlin.

Goring, D.G. & Nikora, V.I. 2002. Despiking acoustic Doppler velocimeter data. *Journal of Hydraulic Engineering* 128(1): 117-126.

Kühn, G. 2007. Untersuchungen zur Feinsedimentdynamik unter Turbulenzeinfluss (´Ínvestigations of the dynamics of fine sediments under the influence of turbulence´). *Dissertationsreihe am Institut für Hydromechanik der Universität Karlsruhe*, Heft 2007/2 (in German).

Lysne, D.K., Glover, B., Støle, H. & Tesaker, E. 2003. Hydraulic Design. *Norwegian University of Science and Technology, Department of Hydraulic and Environmental Engineering*.

Mosonyi, E. 1956. *Water Power Development*. Publishing House of the Hungarian Academy of Sciences, Budapest, Hungary.

Nøvik, H., Dudhraj, A., Olsen, N.R.B., Bishwakarma, M.B. & Lia, L. 2014. Numerical Modeling of Nonuniform Flow in Settling Basins. *Hydro Nepal* 14: 27-35.

Olsen, N.R.B. 1994. SSIIM – A Three-dimensional Numerical Model for Simulation of Water and Sediment Flow. *Proc. 5th International Conference on Hydraulic Engineering Software*, Port Carras, Greece.

Olsen, N.R.B. & Skoglund, M. 1994. Three-dimensional numerical modeling of water and sediment flow in a sand trap. *Journal of Hydraulic Research* 32(6): 833-844.

Olsen, N.R.B. & Kjellesvig, H.M. 1999. Three-dimensional numerical modelling of bed changes in a sand trap. *Journal of Hydraulic Research* 37(2): 189-198.

Ortmanns, C. 2006. Entsander von Wasserkraftanlagen (´Desanding facilities at hydroelectric power plants´). *VAW-Mitteilung 193* (Minor, H.-E. ed.), VAW, ETH Zurich (in German).

Padhy, M.K. & Saini, R.P. 2011. Study of silt erosion on performance of a Pelton turbine. *Energy* 36(1): 141-147.

Paschmann, C., Fernandes, J.N., Vetsch, D.F. & Boes, R.M. 2016. Experimental setup for flow and sediment flux characterization at desanding facilities. *Flow Measurement and Instrumentation* (submitted).

Patt, H. & Gonsowski, P. 2011. *Wasserbau – Grundlagen, Gestaltung von wasserbaulichen Bauwerken und Anlagen ('Hydraulic Engineering – Fundamentals, Design of hydraulic engineering structures and facilities')*. Heidelberg: Springer (in German).

Pope, S.B. 2000. *Turbulent Flows*. Cambridge University Press.

Qamar, M.Z., Verma, M.K. & Meshram, A.P. 2014. Importance of Desilting Basins in Run-of-River Hydro Projects in Himalayan Region. *International Journal of Emerging Technology and Advanced Engineering* 4: 407-412.

Shah, C., Verma, M. & Deolalikar, P. 2008. Transition for De-silting Basin with Open Channel Flow. *ISH Journal of Hydraulic Engineering* 14(1): 117-125.

Simanjuntak, T.; Boeriu, P. & Roelvink, D. 2009. Consideration on the Sedimentation Process in a Settling Basin. *Journal of Hydrology and Hydromechanics* 57(1): 16-25.

Truffer, B., Küttel, M. & Meier, J. 2009. Wasserfassung Titer der GKW – Entsanderabzüge System HSR in grossen Entsanderanlagen (´GKW water intake Titer – HSR flushing system at large desanding facilities´). *Wasser Energie Luft* 101(3): 207-208 (in German).

Wahl, T.L. 2003. Discussion of ´Despiking acoustic Doppler velocimeter data´ by Derek G. Goring and Vladimir I. Nikora. *Journal of Hydraulic Engineering* 129(6): 484-487.

Weerakoon, S. & Rathnayake, U. 2007. Effect of the Entrance Zone on the Trapping Efficiency of Desilting Tanks in Run-of-River Hydropower Plants. *Proc. International Conference on Small Hydropower*, Sri Lanka.

Wren, D.G., Barkdoll, B.D., Kuhnle, R.A. & Derrow, R.W. 2000. Field techniques for suspended-sediment-measurement. *Journal of Hydraulic Engineering* 126(2): 97-104.

FIGURES
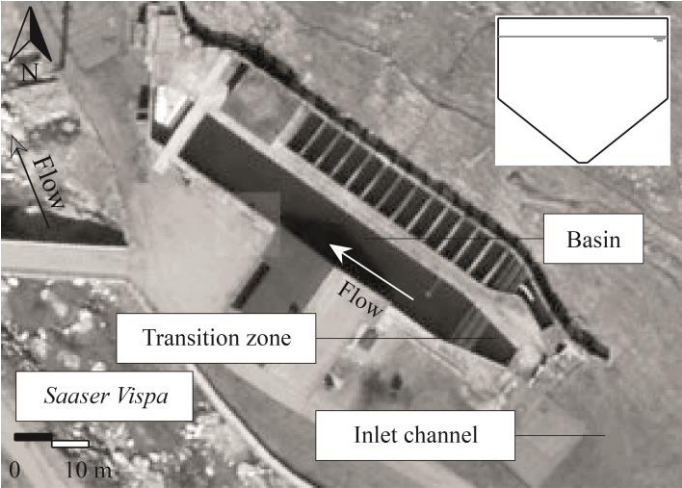
Figure 1. Aerial picture of the desanding facility Saas Balen including schematic basin cross section geometry. Reproduced by permission of swisstopo (JA100120).
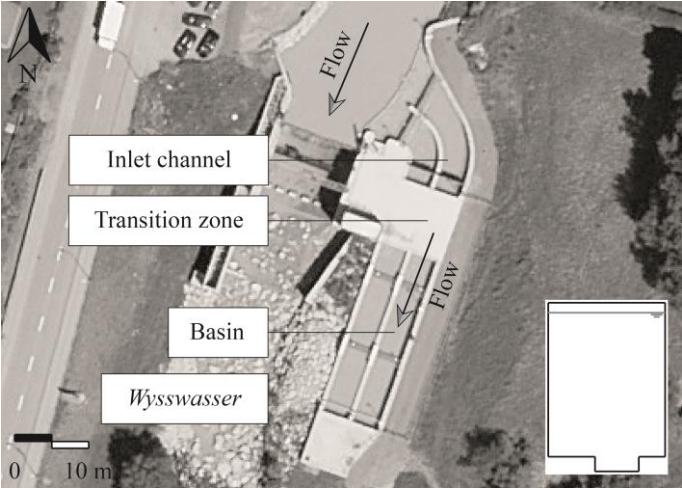

Figure 2. Aerial picture of the desanding facility Wysswasser including schematic basin cross section geometry (downstream view). Reproduced by permission of swisstopo (JA100120).
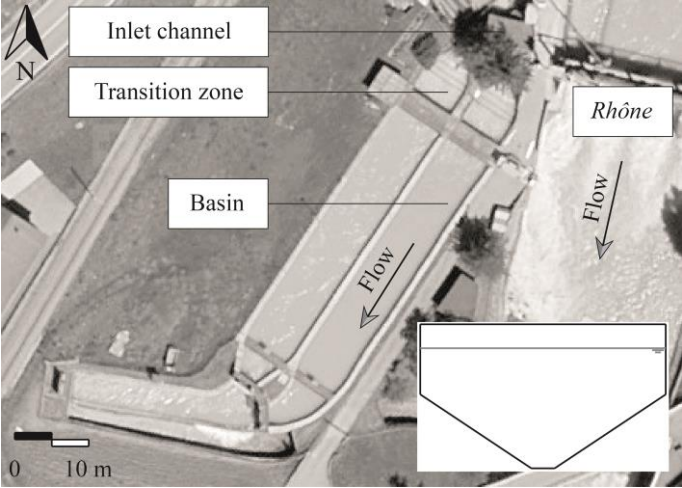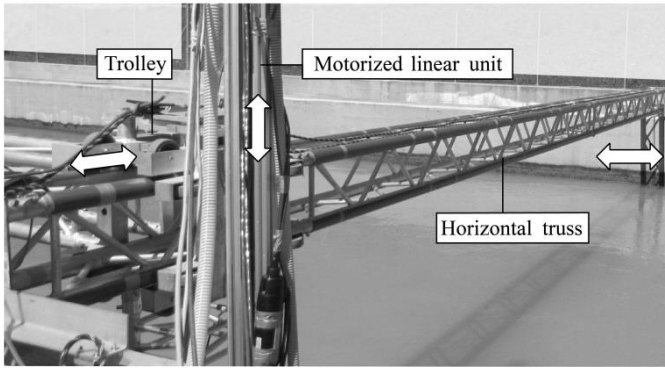

Figure 3. Aerial picture of the desanding facility Moerel in-cluding schematic basin cross section ge-ometry. Reproduced by permission of swisstopo (JA100120).

Figure 4. On-site modular bearing system for the measurement instrumentation; arrows indicate the directions of movement.
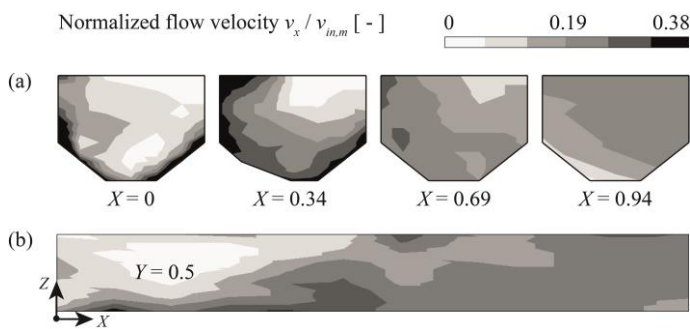
Figure 5. Contour plots of longitudinal flow velocity v_x normalized with mean inlet channel flow velocity $v_{in,m}$ at the facility Saas Balen: (a) Selected basin cross sections, downstream view; (b) longitudinal section at basin centerline, flow from left to right.
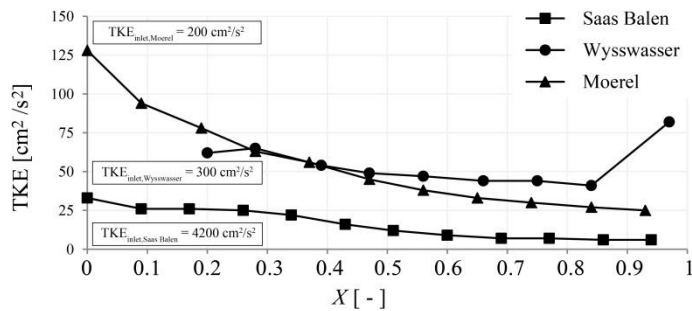
Figure 6. Comparison of cross sectional mean TKE at the facilities Saas Balen (■), Wysswasser (□) and Moerel (▲) and according inlet channel TKE.
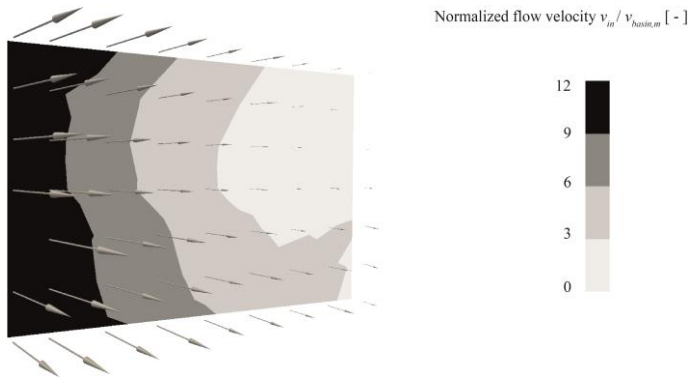
Figure 7. Contour plot of flow velocity magnitude in the inlet channel measurement cross section normalized with basin mean flow velocity at the facility Saas Balen; the vectors represent the longitudinal flow velocity component (upstream view).
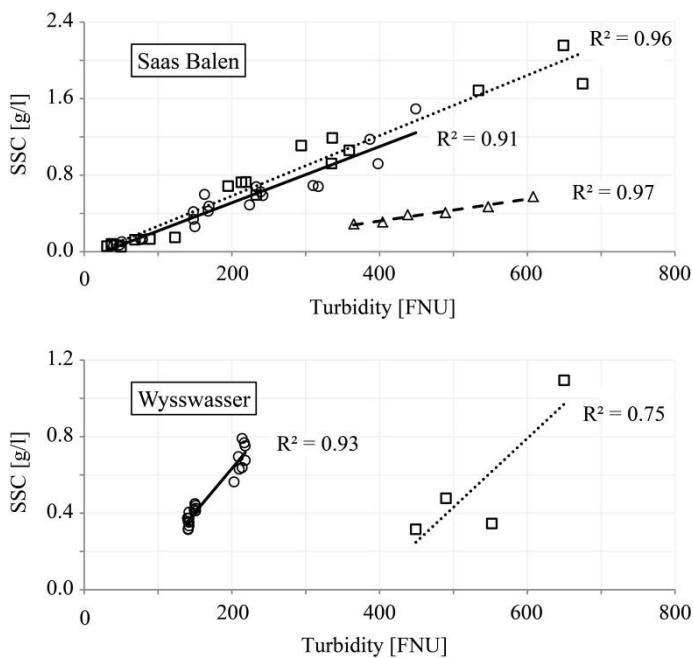
Figure 8. Correlation of turbidity and SSC for the inlet channel (□, dotted), basin (○, solid) and outlet (Δ, dashed) at the facilities Saas Balen and Wysswasser.
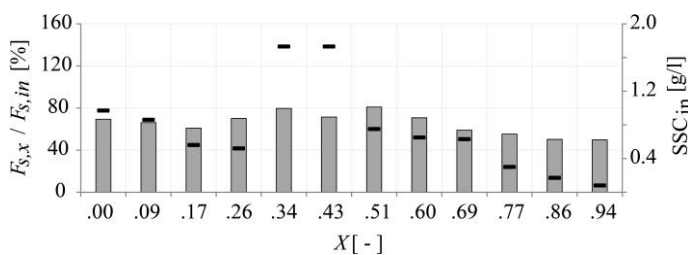
Figure 9. Normalized cross sectional sediment fluxes $F_{S,x}$ / $F_{S,in}$ (columns) and simultaneous mean SSC in the inlet channel (horizontal bars) at the facility Saas Balen.
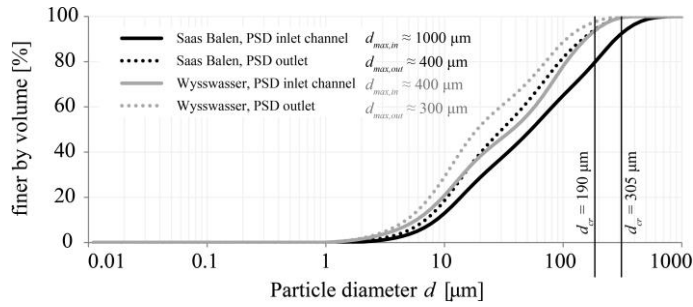
Figure 10. Mean PSD in the inlet channel and at the outlet, and indication of critical grain size d_{cr} at the facilities Saas Balen and Wysswasser during the measurement campaign.
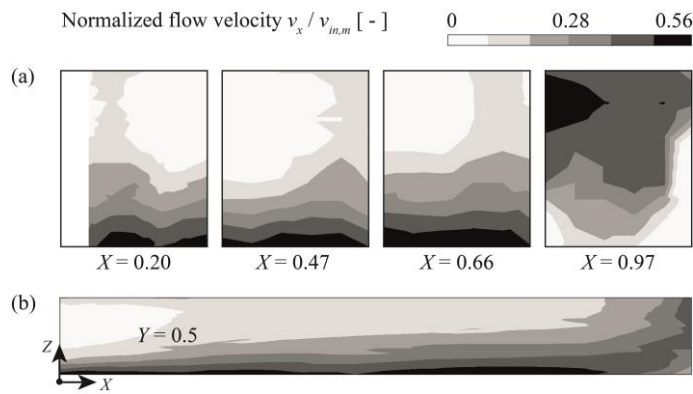

Figure 11. Contour plots of longitudinal flow velocity v_x normalized with mean inlet channel flow velocity $v_{in,m}$ at the facility Wysswasser: (a) Selected basin cross sections, downstream view; (b) longitudinal section at basin centerline, flow from left to right.
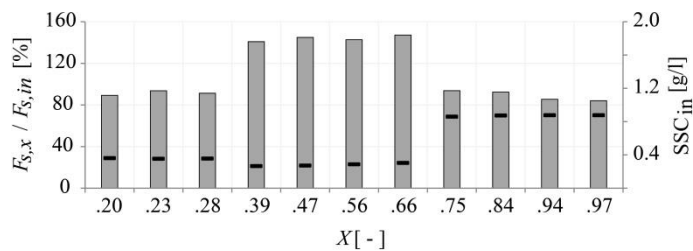

Figure 12. Normalized cross sectional sediment fluxes $F_{S,x} / F_{S,in}$ (columns) and simultaneous mean SSC in the inlet channel (horizontal bars) at the facility Wysswasser.
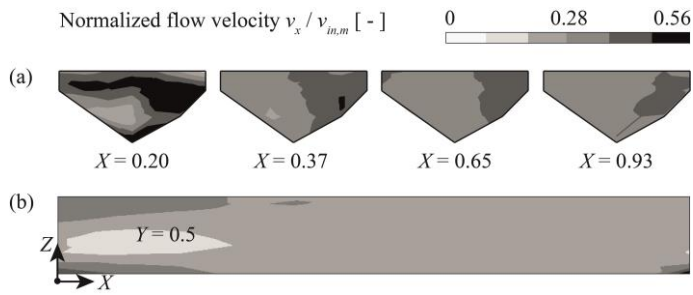
Figure 13. Contour plots of longitudinal flow velocity v_x normalized with mean inlet channel flow velocity $v_{in,m}$ at the facility Moerel: (a) Selected basin cross sections, downstream view; (b) longitudinal section at basin centerline, flow from left to right.
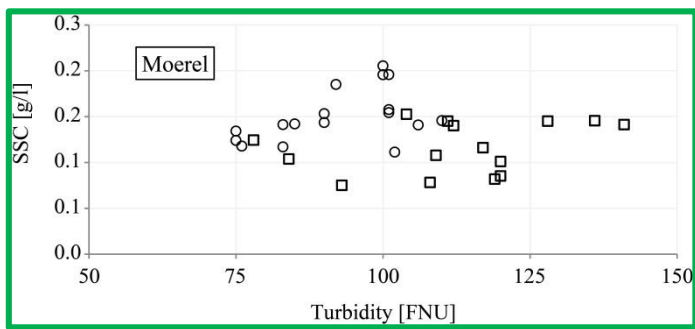

Figure 14. Correlation of turbidity and SSC for the inlet channel (□) and basin (○) at the facility Moerel.
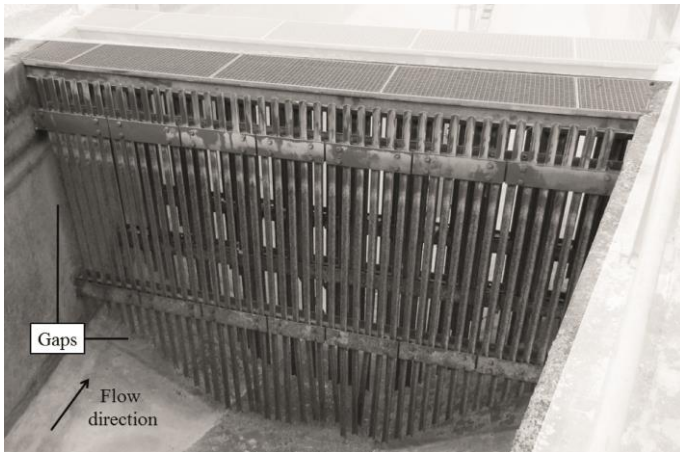

Figure 15. Three rows of tranquilizing racks with V-shaped bars (tips pointing downstream) upstream of the basin at Saas Balen. Source: VAW.

Figure 16. Three rows of tranquilizing racks with V-shaped bars (tips pointing downstream) upstream of the basin at Wysswasser. Source: VAW.